Simulating the Measurement of the Electron Beam Emittance at AWAKE

Patrick Chin

March 25, 2017

Department of Physics & Astronomy,
University College London

Supervised by Prof. M. Wing
& Dr. S. Jolly

Submission of coursework for Physics and Astronomy course PHASM201/PHAS3400

Please sign, date and return this form with your coursework by the **specified deadline** to the Departmental Office.

DECLARATIONOFOWNERSHIP

I confirm that I have read and understood the guidelines on plagiarism, that I understand the meaning of plagiarism and that I may be penalised for submitting work that has been plagiarised.

I confirm that all work will also be submitted electronically and that this can be checked using the JISC detection service, Turnitin®.

I understand that the work cannot be assessed unless both hard copy and electronic versions of the work are handed in.

I declare that all material presented in the accompanying work is entirely my own work except where explicitly and individually indicated and that all sources used in its preparation and all quotations are clearly cited.

Should this statement prove to be untrue, I recognise the right of the Board of Examiners to recommend what action should be taken in line with UCL's regulations.

Signed ______________________________

Print Name ______________________________

Dated ______________________________

Title	Date Received	Examiner	Examiner's Signature	MARK

University College London, Gower Street, London WC1E 6BT
Tel: +44 (0)20 7679 2000
email@ucl.ac.uk
www.ucl.ac.uk

Abstract

In preparation for runs at AWAKE in CERN, simulations of the beam and measurement of beam parameters with a spectrometer were carried out. This was done in order to investigate how the spectrometer behaves under changes to experimental parameters. The energy spreads of the beam were tested and a percentage energy spread of $4\,\%$ was found to be the cutoff point at which measurements become reliable. Emittance values were tested and emittances above $10^{-5}\,\mathrm{m\,rad}$ were found to be inaccurate. Background photon values up to 10^4 times the expected background were simulated, showing accurate measurements up to a factor of $\sim 4 \times 10^2$, above which the measured emittance deviated significantly from the true value.

Contents

1 Introduction

Advancements in quantum and particle physics are primarily driven by experimental observations which can verify or refute previous hypotheses, or can provide data from which new hypotheses can be drawn, with the overall goal of helping us have a deeper understanding of the universe around us. Particle colliders are a main source of observational data at the quantum scale, and can create millions of collision events every second. Design modifications to these colliders mostly increase the luminosity of the collision in order to increase the collision rate and produce more data. This report however, focuses on a design modification aimed at increasing the energy of the colliding beams. Increasing the energy of particle colliders will give the ability to investigate energy regions yet to be reached and allow the observation of interactions that only happen at higher energies. These interactions may give insight into questions pertaining to the unification of the fundamental forces.

Proton–proton beam energies at the Large Hadron Collider (LHC) have recently reached energies of 13 TeV [8], whereas lepton–lepton colliders have yet to reach the TeV energy scale. The largest lepton–lepton collider, the Large Electron-Proton Collider (LEP), was closed down to make way for the LHC in 2000 after having reached a maximum energy of 209 GeV [3].

The appeal of colliding leptons over composite particles such as protons arises from the fact that leptons are fundamental point-like particles. Their centre-of-mass energy is more easily determined and produce a much cleaner environment on collision, allowing for easier analysis of data as less interactions need to be taken into account.

One of the drawbacks to circular accelerators, is the loss of a particle's energy due to synchrotron radiation. This is the emittance of radiation from relativistic charged particles that are moving in a uniform magnetic field. The energy loss is inversely proportional to the fourth power of the rest mass of the particle [18], meaning that electrons lose more energy than protons by a factor of about 10^{13} which is. During experiments performed at the LEP the radiated power when running at 100 GeV reached about 18 MW which needs to be resupplied to the beam.

This continuous loss of energy can be overcome by creating linear particle accelerators. There are currently two radio-frequency (RF) linear lepton–lepton accelerator proposals, the Compact Linear Collider (CLIC) [12] and the International Linear Collider (ILC) [4] which are expected to reach collision energies of up to several TeV and 500 GeV respectively. Both collaborations have recently joined efforts under the Linear Collider Collaboration. The continuous scaling of linear accelerators to higher and higher energies, with current RF technology requires greater accelerator lengths reaching lengths extending to the 100 km scale. Building accelerators of this scale is deemed impractical for most situations due to geographical and financial limitations. This urges the development of new technologies in order to continue pushing the energy frontier of particle accelerators while scaling down the accelerator lengths.

2 Plasma Wakefield Acceleration

Current RF accelerator technology is limited to an electromagnetic gradient of about 100 MeV m^{-1} due to material breakdown in the walls of the structure. The ability of plasma to sustain very large electromagnetic fields makes it a good candidate for a medium within which charged particles can be accelerated. The concept being that the plasma can act as an energy transfer medium, removing energy from a driver beam, such as a laser or a proton beam, and transferring it to a bunch of charged leptons. As the driver beam travels through the plasma cell, it leaves an oscillating electromagnetic field in it's wake. The beam to be accelerated (the witness beam) is injected ahead of a propagating electromagnetic field as shown in Figure 1b where it is accelerated under the electromagnetic gradient. In 1979, the concept of laser plasma acceleration was shown in simulations to be of practical use in accelerators and pulsers [19]. More recently, proof-of-concept experiments implementing laser plasma acceleration have been shown to accelerate electrons to the GeV scale in a cm-scale plasma cell [14, 11], providing results that are consistent with simulations.

2.1 The AWAKE Project

Simulations of plasma wakefield accelerators driven by proton beams were carried out in 2009 [7], showed the high energy transfer efficiency between a driver proton bunch and an electron witness bunch. In these simulations, a 1 TeV proton beam drove the wakefield in a 400 m long plasma cell, which accelerated a 10 GeV electron beam to 650 GeV. The AWAKE project is a proof-of-concept experiment for proton driven plasma wakefield acceleration with the goal of accelerating 15 MeV electrons up to ∼1.3 GeV over a distance of 10 m. Later, aiming to reach 10 GeV in the same distance. This will demonstrate the use of electromagnetic gradients that are about 10 times larger than current RF acceleratrs.

A few challenges arose in the design of this experiment and are discussed next.

2.1.1 Proton Bunch Length

The first challenge in the development of this accelerator was getting the length of the proton driver bunch small enough such that it is able to create resonant waves in the plasma. Typical proton bunches such as those produced by the CERN Super Proton Synchrotron (SPS), have lengths of $\sim$ 10 cm which alone, cannot create strong plasma waves at the required wavelength in the mm scale as the Fourier component of the proton beam at the plasma frequency is negligible. Simulations [10] on the compression of these proton bunches to such small distances, show that reducing the longitudinal phase volume blows up the transverse phase volume, resulting in a diverging beam with a large emittance. An alternative method would be to split up the proton bunch into a number of micro-bunches to be simultaneously decelerated, all of which contribute energy to the wakefield.

The splitting of the proton beam can be achieved by using an instability between the beam and the plasma arises from the mutual amplification of the rippling of the beam radius and the plasma wave, known as self-modulated instability (SMI). This instability tends to destroy the plasma wave as the amplification focuses and defocuses various parts of the beam. However, by seeding the SMI with a short electron bunch [13], a laser pulse [17] or a sharp cut in the bunch profile [10], a single mode of the oscillating plasma wave and beam rippling will be promoted while others will be suppressed. This produces well-separated micro-bunches of protons with of a short enough length to induce a plasma wave at the resonance frequency of the plasma. The plasma wavelength is $\lambda_{pe} \approx 1.26$ mm meaning that the 10 cm proton bunch will have to be split into $\sim$ 100 micro-bunches in order to be able to drive the wake.

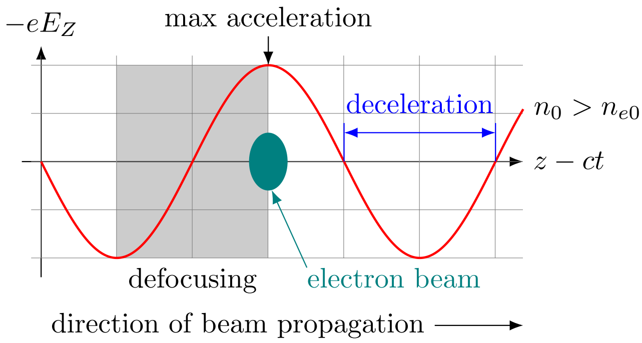

(a) Injection of the electrons for a shorter plasma wavelength, where electrons may crest the wave.

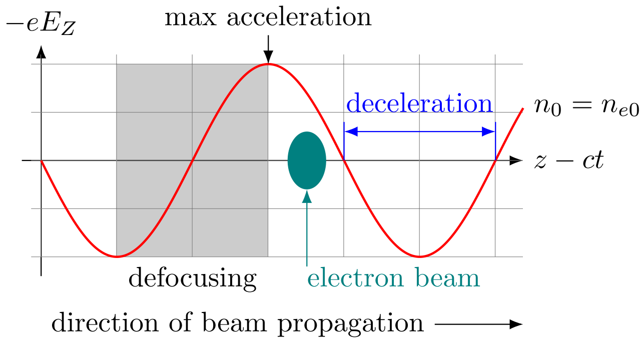

(b) Injecting at the ideal phase, where all electrons will be accelerated.

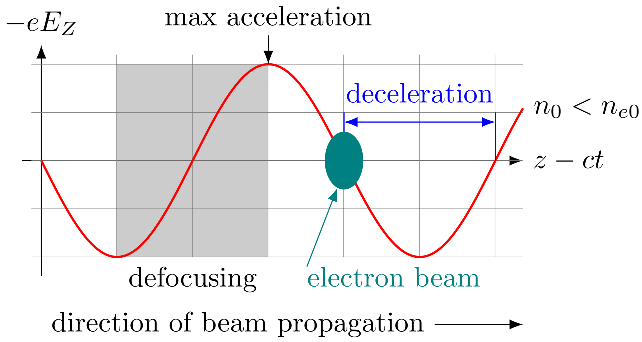

(c) Injection for a longer plasma wavelength, where electrons may fall into the deceleration region.

Figure 1: Phase of the injection of the electron beam [22].

2.1.2 Uniform-Density Plasma Cell

All proton micro-bunches contribute to the wakefield, and only if the plasma density is uniform, will the contribution of each bunch be coherent. Incoherent proton bunches will cause alterations in the plasma wakefield meaning the electron bunches arrive at the wrong phase of the plasma oscillation.

An increase in the plasma density will shorten the plasma wavelength causing the electron bunch to crest plasma wave it was riding and fall into the defocusing phase of the plasma wave as shown in Figure 1a. A decrease in the plasma density will increase the plasma wavelength causing the plasma wave to fall further behind the electron bunch meaning the electron bunch to fall into the trough of the plasma wave resulting in a deceleration of the electron beam 1c. The electron beam must be in the region of length $\lambda_{pe}/4$ between the defocusing and decelerating phases of the plasma wave in order to be appropriately accelerated. These effects also affect the proton beam, however due to their large longitudinal momentum these effects are significantly larger for the electrons.

This requirement of the plasma limits the plasma selection to being uniform rubidium vapor, ionised by a co-propagating laser pulse [15, 16]. Rubidium was chosen due to it's low ionization potential and heavy atomic mass. A heavy element is required to minimize the movement of the plasma's nuclei which causes adverse effects on the plasma's behaviour [21, 20]. The Rubiduim vapor is kept in thermodynamic equilibrium at a constant temperature and volume.

2.1.3 Injection of the Witness Beam

Due to SMI, the shape of the drive beam changes in the plasma and for the first four meters, the difference between the phase velocity of the wakefield and the proton beam velocity is quite large and this will effect the electron beam in the same manner as having a non uniform plasma, detailed above. To avoid this problem it was suggested that the electrons could be injected into the plasma after SMI had fully developed. The design of the injection method arrived at passing the electron beam through a narrow vacuum tube separated from the plasma by a thin foil. Then after $\sim 4\,\mathrm{m}$ the electrons will be directed into the wakefield close close behind the proton driving beam.

2.1.4 AWAKE Overview

The SPS will provide a 400 GeV proton beam with a bunch length of $\sigma_z = 12\,\mathrm{cm}$ and an intensity of $\sim 3 \times 10^{11}$ protons per bunch. This will travel down the 750 m long proton beam line, previously used for the CERN Neutrinos to Gran Sasso project (CNGS), and will be focused infront of the plasma cell to a horizontal and vertical beam size of $\sigma_{x,y} = 200\,\mu\mathrm{m}$. This beam will then enter the 10 m long Rubiduim vapor plasma cell with an adjustable density at the 10^{14} to 10^{15} electrons/cm scale.

The proton driver will self modulate at the plasma wavelength λ_{pe} after being seeded by a high powered $\approx 4.5\,\mathrm{TW}$ laser pulse that is co-axial and co-propagating with the proton driver beam. This laser also serves the purpose of ionising the Rubidium vapor to create the plasma. For these beams to be co-axial for the full length of the plasma cell, they need to be synchronous to within 100 ps and the size of the focal point of the proton beam is required to be $\leq 100\,\mu\mathrm{m}$ and $\leq 15\,\mu\mathrm{rad}$

The electron witness beam will be created via photo-emission by an illuminating cathode electron source and accelerated by a 2.5 cell RF-gun and a meter long booster at 3 GHz.

3 Spectrometer

There are two main goals the spectrometer is expected to fulfill. The first is to measure the mean energy and energy spread of the beam as is it this measurement of the mean energy that determines the success of the AWAKE project, whether or not the electrons were accelerated up to the desired 10 GeV.

3.1 Design

4 Theory

4.1 Single Particle Dynamics

When working with beams of particles, it is advantagous to work in the coordinate system that follows the ideal path of the beam. If the beam's motion in the x and y planes are independent, i.e. we ignore coupling terms, the each particle's motion in each plane can be described by

$$\begin{pmatrix} u(z) \\ u'(z) \end{pmatrix} = \begin{pmatrix} C_u(z) & S_u(z) \\ \sqrt{C_u'(z)} & S_u'(z) \end{pmatrix} \begin{pmatrix} u_0 \\ u_0' \end{pmatrix} \tag{1}$$

where u is either x or y and u' is the transverse velocity of the particle in the u plane. The coordinate (u, u') lies in what is known as phase space. Using

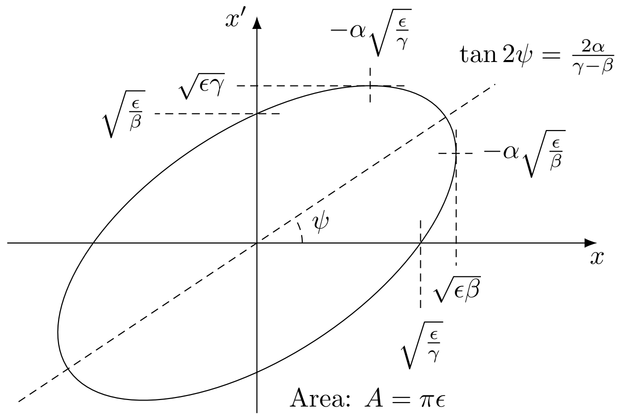

Figure 2: A representation of the relation between the Twiss parameters of a beam's ellipse in phase space [22].

this system of matricies the drift and quadrupole matricies can be derived [22]. The drift matrix is

$$\mathcal{M}_D(l) = \begin{pmatrix} 1 & l \\ 0 & 1 \end{pmatrix} \tag{2}$$

the focusing quadrupole matrix is

$$\mathcal{M}_{QF}(l) = \begin{pmatrix} \cos\psi & \frac{1}{\sqrt{k}}\sin\psi \\ -\sqrt{k}\sin\psi & \cos\psi \end{pmatrix} \tag{3}$$

and the defocusing quadrupole matrix is

$$\mathcal{M}_{QD}(l) = \begin{pmatrix} \cosh\psi & \frac{1}{\sqrt{|k|}}\sinh\psi \\ -\sqrt{|k|}\sinh\psi & \cosh\psi \end{pmatrix} \tag{4}$$

These transport matricies can be multiplied together resulting in the transformation matrix representing a path containing all accelerator components making it simple to follow a particle through a transport line.

4.2 Emittance

Grouping the individual particles in a particle beam, they will occupy an area in phase space known as the emittance. Qualitatively the emittance of a beam is a measure of how parallel the particles of the beam are to each other. It is a conserved quantity while the beam is not being acted upon by external forces.

In phase space the beam of particles will usually take up an area resembling that of an ellipse. This is because, after a diverging or converging beam has traveled through an apeture, we expect particles that are further away from the centre of the beam to have a larger transverse momentum. This is unless the beam is being measured at it's waist where it is transitioning between converging and diverging or visa versa. Figure 2 shows the projection of a diverging beam onto a two dimensional phase plane, called the phase ellipse. The line that defines the ellipse is drawn such that 95 % of all the particles in the beam are contained [6]. The emittance is defined by the area of this ellipse divided by π in units of m rad. Note that in general the transverse momenta, hence the slope of the particles in the beam, are very small so the approximation $\sin u' \approx u'$ can be used.

The general equation of an ellipse can be used to describe the phase ellipse:

$$\gamma x^2 + 2\alpha x x' + \beta x'^2 = \epsilon \tag{5}$$

where α, β, γ and ϵ are ellipse parameters that determine the ellipse's shape and orientation in phase space, where ϵ, the area of the ellipse is the emittance [1] Of the four beam parameters, only three are independant and since ϵ is defined as the area, the other three can be found to be correlated from the ellipse's geometric properties by

$$\beta\gamma - \alpha^2 = 1 \tag{6}$$

By expressing this ellipses as a matrix, transformation rules have been derived to transport the beam [22]. The beam matrix can be defined by

$$\boldsymbol{\sigma} = \begin{pmatrix} \sigma_{11} & \sigma_{12} \\ \sigma_{21} & \sigma_{22} \end{pmatrix} = \epsilon \begin{pmatrix} \beta & -\alpha \\ -\alpha & \gamma \end{pmatrix} \tag{7}$$

where each element describes distributions of particles in the beam as follows:

$$\sigma_{11} = \langle x_i^2 \rangle = \epsilon\beta \tag{8}$$

$$\sigma_{22} = \langle {x'}_i^2 \rangle = \epsilon\gamma \tag{9}$$

$$\sigma_{12} = \langle x_i x_i' \rangle = -\epsilon\alpha \tag{10}$$

The evolution of this matrix along the beam transport line can then be described by

$$\boldsymbol{\sigma}_1 = \mathcal{M}\, \boldsymbol{\sigma}_0\, \mathcal{M}^T \tag{11}$$

5 The Simulation

The simulation of this experiment was split into three parts: the simulation of the beam, the simulation of the effects of the background and camera,

[1]Often, the units of π are omitted and the emittance is given in units of π m rad.

Parameter	Value
Screen and Camera	
Screen width	1 m
Screen height	65 mm
Horizontal pixels	1850
Screen efficiency	5000 photons/electron
Camera acceptance	1.5×10^{-5}
Camera MCP Gain	1442
Camera quantum efficiency	0.15
Accelerated electron beam	
Emittance (ϵ)	1×10^{-6} m rad
β	1 m
α	0.5 rad
Mean energy $(\bar{E})$	1.3 GeV
Energy spread (σ_E)	0.4 GeV
Electrons/bunch (N_{e^-})	1×10^9
Background photon density	$3.415 \times 10^4\,\mathrm{m}^{-2}$

Table 1: The expected values for many experimental parameters have been calculated.

and the reconstruction of the beam to measure the parameters of the beam.

5.1 The Electron Beam

Given enough computing power and time, the simulation of the beam from, the end of the plasma cell, passing through two quadrupoles and through a dipole could have been done on BDSIM [1], a Geant4 [2] toolkit for simulating radiation traveling through an accelerator. This software package simulates a each particle individually, updating it's position and velocity at each step through the accelerator by applying the effect of forces from all fields within the accelerator. For beams consisting of $\sim 10^9$ particles, tracking each particle individually as they travel down the beam line would take enormous amounts of time and available computing power, and as many simulations were required to be performed this would have been impractical for obtaining any reasonable amount of data.

A new program was written, taking advantage of beam matrices to describe the beam as a whole. The goal of the first part of this program is to simulate the intensity of the incident beam at each pixel on the screen.

5.1.1 BDSIM Calibration

The effect of the quadrupole and the dipole are dependant on the energy of the individual electrons in the beam. So to calculate the density of an electrons along with their energies as a function of the horizontal screen position a number of BDSIM simulations were run. 10^5 electrons where fired individually down the simulated AWAKE beam line. These electrons had a square energy distribution from 0 TeV to 10 TeV, and had a Gaussian spacial distribution with $\sigma_x = \sigma_y = 6$ mm, and no transverse momentum hence zero emittance. This large energy range was chosen as to encompass the entire energy range that would hit the screen. The dipole was set to it's highest setting of 650 A to achieve the maximum spread of the beam on the screen.

These BDSIM runs were used to plot the function in Figure 3a which shows the relationship between the electron energy and where is it expected to hit the screen. Figure 3b is an example of the horizontal distribution of a beam of electrons with a Gaussian energy spread onto the screen. This was calculated by applying the inverse of the function $E(x)$ shown in Figure 3a, to the energy distribution of the beam.

At these experiment settings, the entire of the beam electrons hit the screen allowing for a more accurate measurement of the beam parameters. The

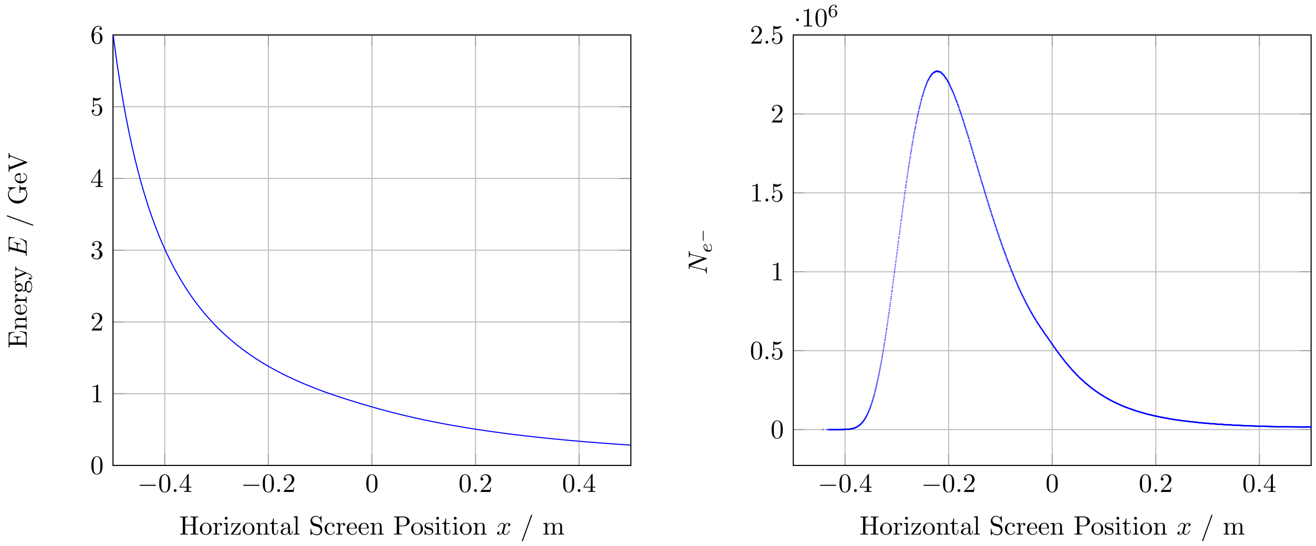

(a) Electron energies corresponding to the horizontal screen position due to the effect of the dipole.

(b) The number of electrons expected to hit the screen at each x position for $E = 1.3\,\mathrm{GeV}$ and $\sigma_E = 0.4\,\mathrm{GeV}$.

Figure 3: The functions $E(x)$ and $N_{e^-}(x)$ extracted from the BDSIM calibration output data. These functions are used to calculate the horizontal spread of the electrons across the screen.

effect of the emittance and quadrupoles on the horizontal spread is taken to be negligible in comparison to the effect of the dipole, and so it's effect is taken into account by adding a horizontal smearing to the horizontal position of each electron on the screen. This results in this plot being all that is required to simulate the transverse spread of the beam.

The drift distances from the second quadrupole to the screen were also recorded for each x position on the screen. This function $d(x)$ is used in the calculation of the vertical beam size, discussed next.

5.1.2 Deriving the Beam Size Function

The dipole spreads the beam horizontally across the screen. The electrons in each vertical strip of pixels are grouped together and their energy approximated to be equal. This is allowed as the energy spread in each strip will always be less than 0.5 %. This was calculated from data used to plot Figure 3a, by finding the ratio between the difference in energies between adjacent strips, by the energy value at that strip. This was done for all strips and the maximum value was a 0.5 % difference in energy.

Using this assumption, we are able to create one beam and transport matrix for electrons in each vertical stream of pixels. The root mean square of the vertical beam size on the screen can be extracted from the resultant beam matrix σ_1. To arrive at this beam matrix, the transport matrix $\mathcal{M}$ is applied to the initial beam matrix σ_0 in (11). The transport matrix is the product of the transport matrices of each component of the spectrometer:

$$\begin{aligned} \mathcal{M} = \mathcal{M}_D(d) \cdot \mathcal{M}_{QD}(l_2) \cdot \mathcal{M}_D(g_2) \\ \cdot \mathcal{M}_{QF}(l_1) \cdot \mathcal{M}_D(g_1) \end{aligned} \tag{12}$$

where $\mathcal{M}_D(d)$ is the drift transport matrix which is a function of the travel distance and $\mathcal{M}_{QD}(l)$ is the transport matrix of the quadrupole. g_1 is the drift distance (the gap) between the end of the plasma cell and the first quadrupole, g_2 is the gap between the two quadrupoles, l_1 and l_2 are the effective quadrupole lengths of the focusing and defocusing quadrupoles respectively. d is the drift distance between the second quadrupole and the screen, taking into account the effect of the dipole, hence, is a function of the energy. The shape of this function was calculated in the BSDIM runs.

For simplicity, it is assumed that the quadrupoles strengths k_1 and k_2 are set to values such that each quadrupole focuses at the mean energy of the beam, hence these variables are proportional to the beam's mean energy.

Applying the matrix multiplication results in the vertical beam size as a function of the horizontal screen position:

$$\sigma_y^2 = \sigma_{1,11} = C^2(x)\sigma_{0,11} + 2C(x)S(x)\sigma_{0,12} + S^2(x)\sigma_{0,22} \tag{13}$$

After generating, a two dimensional histogram representing the number of electrons hitting the screen at each pixel the goal is to simulate the effectiveness of the equipment and translate this number to represent the raw signal that will be read off for each pixel.

5.2 Backgrounds

How good the measurement of the emittance is, is most dependant on the magnitude of the multiple sources of backgrounds as well as the reliability of the equipment. The following sources of error were taken into account: the efficiency of the scintillator screen, the acceptance of the camera due to it's distance from the scintillator screen, the background photon density, the emittance of photoelectrons in the camera, the thermal noise in the camera, the amplification by the microchannel plate (MCP) and the readout noise. Each source of noise is added to each pixel independently.

The first two error sources, the scintillator screen and the camera acceptance, both scale the signal. So for each electron that hits the screen, it is expected that an average of 5000 photons are to be emitted. The camera acceptance, is the ratio of photons that the camera registers to the number of photons emitted by the scintillator, with a value of 1.5×10^{-5}. After the addition of these two effects, the camera is expected to receive 7.5 % of the original electron signal. The expected value for the number of photons incident on the camera due to the beam electrons is a Poisson random number.

It is assumed that there is a uniform distribution of photons incident on the camera. The density of these electrons is expected to be $3.415 \times 10^4\,\mathrm{photons/m^2}$ equating to 0.01 background photons per pixel during the $3 \times 10^{-3}\,\mathrm{s}$ the gate is open. The number of background photons that hits a pixel is a discrete value, and so is also generated by generating a Poisson random number. As discussed later in Section 6 this value is very small in comparison to the signal produced by the beam and will only have an effect if the density of background photons is multiple magnitudes larger than the expected value.

The camera's photomultipliers then convert the photons of light back to an electrical current. This multiplies the incident number of photons by the quantum efficiency of the camera, 0.15. thermal photoelectrons per pixel per second is expected to be 0.016 [9], with the camera running at the expected temperature of $-30\,°\mathrm{C}$ with $16\,°\mathrm{C}$ cooling water and an ambient room temperature of $16\,°\mathrm{C}$. This value is typically doubles for each $5\,°\mathrm{C}$ rise in temperature of the camera [9]. At these running temperatures of the camera, about 9 photoelectrons are expected to be generated during the time the gate is open, which is an insignificant proportion in comparison to the beam signal, creating 1×10^7 photoelectrons before MCP amplification.

The microchannel plate amplifies the number of photoelectrons by 1442, also amplifying all previously added backgrounds as well. This was simulated by scaling the value of the bin, and it's error, by 1442 rather than generating a Poisson random number. The modelling of this process may not be reflect the true nature of this process due to an uncertainty in underlying process, however the overall effect remains accurately simulated. Despite this, the error arising from this process is likely to scale the error as mentioned.

And finally, before the values of the signal is obtained, a readout noise is added. This background is expected to add 7.2 readout electrons per image pixel for the camera operating at 1 MHz.

5.2.1 Error Calculations

Poisson statistics were used for the calculation of errors. Once the shape of the incident beam on the screen was calculated the number of electrons incident on each pixel was given an error of the square root of the count. Two methods of error propagation were used depending on the nature of the process involved. The following processes were modeled as additive processes: background photons hitting the screen, the thermal electrons from the currents in the camera and the readout noise, whereas the multiplicative processes are: photon generation at the scintillator screen, photoelectron generation in the camera PMTs and the amplification of the electron signal by the MCP.

Basic error propagation techniques were used here. For the additive processes, where the new value of each bin n is the sum between the old bin value n_0 and the value given by the process n_{proc}: $n = n_0 + n_{\mathrm{proc}}$ the propagation of error is given by calculating the hypotenuse of the absolute errors:

$$\Delta n = \sqrt{\Delta n_0^2 + \Delta n_{\mathrm{proc}}^2} \tag{14}$$

where the error of a Poisson random number is the square root of the value.

For the multiplicative processes, i.e. $n = \lambda_{\mathrm{proc}} n_0$ where λ_{proc} is the scaling factor of the process the propagation of the error is given by calculating the hypotenuse of the percentage errors:

$$\Delta n = n\sqrt{\left(\frac{\Delta n_0}{n_0}\right)^2 + \left(\frac{\Delta \lambda_{\mathrm{proc}}}{\lambda_{\mathrm{proc}}}\right)^2} \tag{15}$$

Many of the errors Δn_{proc} and $\Delta \lambda_{\mathrm{proc}}$ were unavailable at the time of simulation. All background noises are modeled as uniformly distributed Poisson random numbers so under these assumptions the associated error on each value can correctly be taken to be the square root of the value. For multiplicative processes the resultant values were also Poisson random numbers meaning (15) can be rewritten as

$$\Delta n = n\sqrt{\left(\frac{\Delta n_0}{n_0}\right)^2 + \left(\frac{\sqrt{n}}{n}\right)^2} \tag{16}$$

where the full statistical error of the generated value is taken into account without knowledge of the error of the scaling factor.

5.3 Calculating the Emittance

The signal received from the camera is required to be scaled back to represent the real beam size on the screen. The effect of background and scaling processes are reverted in the reverse order of their application. This is a trivial process done simply by scaling the value

The vertical beam size function used to simulate the shape of the incident electron beam is then fit to the measured beam sizes. The fitting is done wholly by CERN ROOT's χ^2 minimising fitting algorithm [5], using the three beam parameters ϵ, β and γ as parameters to be minimised.

6 Results

Along with the χ^2 minimised parameter values of the fit, each simulation generated a plot, showing the simulated, measured and fitted vertical beam size functions as a function of horizontal position x on the screen. Figure 4 is the output of a run with all parameters set to their expected values. Figure 5 is an output plot for a run with a small (1 %) energy spread so the spread of the beam is very narrow across the screen, so this plot is essentially zoomed in at a small section of the screen. The solid black line is the shape of the simulated electron beam that hits the screen, the black points show the simulated measurements of the RMS width of the fitted Gaussian for each vertical strip of pixels. The blue dashed line is the beam size function fitted to the points.

6.1 Binning errors

After the investigation of multiple experimental parameters, the emittance measurement consistently converged to a value 1×10^{-8} larger than the input emittance. The reason for this systematic error was found to be due to the discretization of the beam hitting the screen meaning that the measurement of the vertical beam size was consistently overestimated. Since the electrons in each pixel are not uniformly distributed but rather more densely distributed closer towards the mean value, giving rise to a systematic overestimation of the vertical beam size of up to two times the vertical size of the pixel. This effect can be seen most clearly when a very small energy spread was used as can be seen in Figure 5, where the measured beam heights are consistently larger than the actual beam height.

This systematic error is displayed in subsequent plots as a blue line, where the red line shows the true beam emittance and the blue line represents where the emittance measurement should be taking into account this error.

6.2 Energy Spread

Initially, the mean energy of the beam and energy spread of the beam were tested independently. Simulations for all combinations of the following energies $E \in \{0.5, 1, 1.3, 2.0, 3.05.0\}$ and the following energy spreads $\sigma_E \in \{0.01, 0.1, 0.3, 0.4\}$ were run. These energies and energy spreads were chosen such

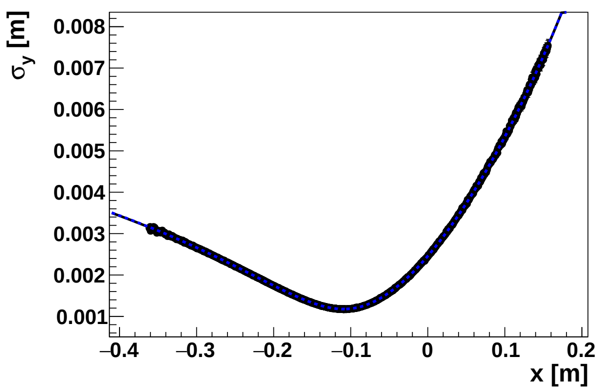

Figure 4: The beam reconstruction (blue line) of a simulation run with all the expected parameter values. $E = 1.3\,\mathrm{GeV}$, $\sigma_E = 0.4\,\mathrm{GeV}$, $\epsilon = 1\,\mathrm{mm\,mrad}$

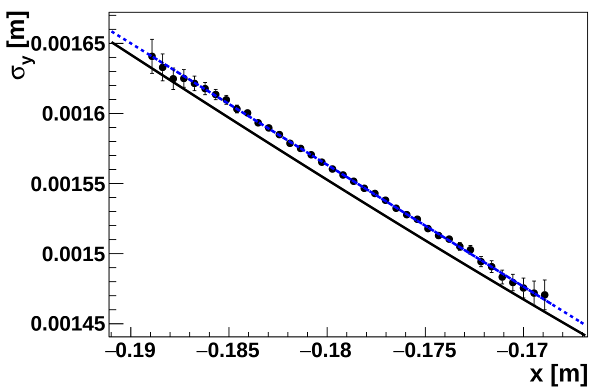

Figure 5: The beam reconstruction, consistently overestimates the vertical beam size. This run used a small percentage energy spread of 1 %*. With all other parameters set to their expected value.*

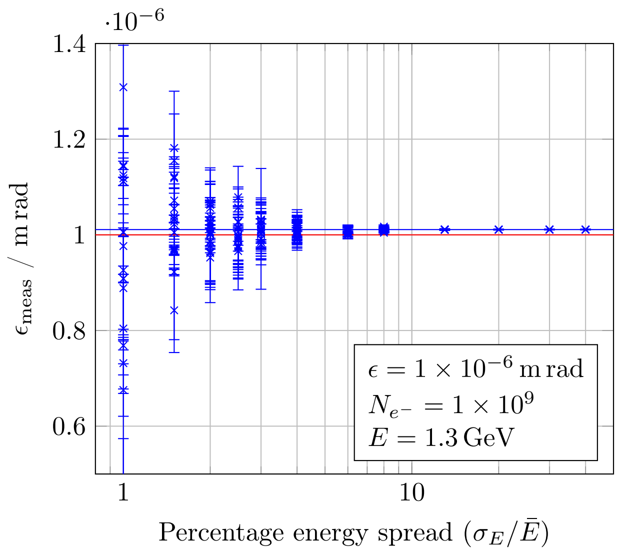

Figure 6: Plot of the simulated emittance measurement against the percentage spread of the beam energy, showing emittance measurements becoming unreliable at percentage energy spreads below 2 %*.*

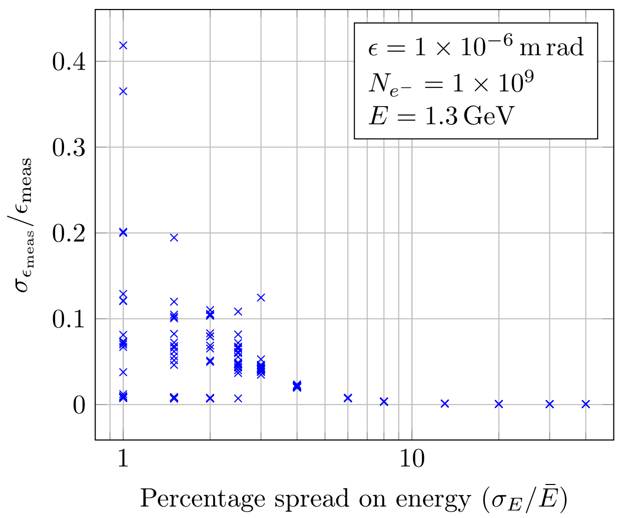

Figure 7: Plot of the simulated emittance measurement errors against the percentage spread of the beam energy, showing an exponential increase in the spread of the errors as the percentage error spread is narrowed.

that at least one full standard deviation of the beam hit the screen. As Figure 3a shows, the range of energies that hit the screen for this setting of the dipole and quadrupole, is from ∼0.28 GeV to 6 GeV.

The smaller the energy spread of the beam the smaller the spread of the beam across the screen. Figure 5 is a plot showing the full spread of the beam across the screen for a beam energy spread of 1 %. The fewer vertical beam measurements that the function is able to fit to, the larger the errors of fitting will be, so the relationship between the errors of the measured emittance and the energy spread in Figure 6 is the expected result. The expected energy spread, 0.4 GeV, translates to a percentage energy spread of 30 % at the expected beam energy of 1.3 GeV. By this point, the error on the measurement of the emittance has converged to less than a 1 %.

Plotting the absolute simulated measurement error against the percentage energy spread in Figure 6 it is clearer the manner in which the errors blow up for lower energy spreads. For lower energy spreads, all measurement errors were expected to increase exponentially. However this is not the case, but rather, the *spread* of measurement errors increased exponentially, meaning that may measurement er-

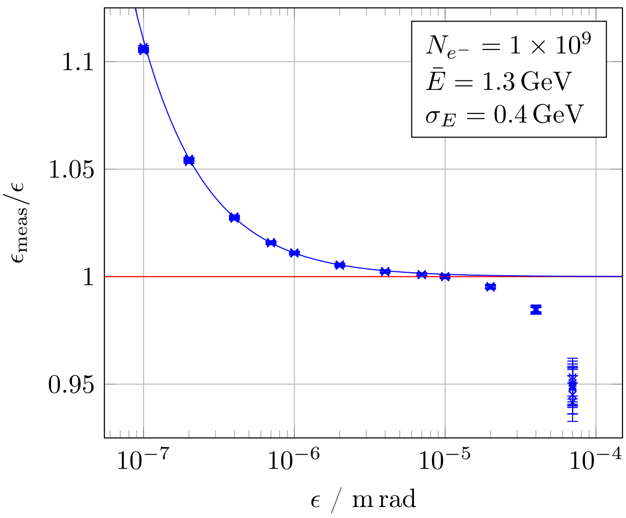

Figure 8: Plot of the ratio between the measured and true emittances of the beam against the true emittance of the beam. The blue line is the expected measurement value when taking into account the systematic overestimation due to discrete bins.

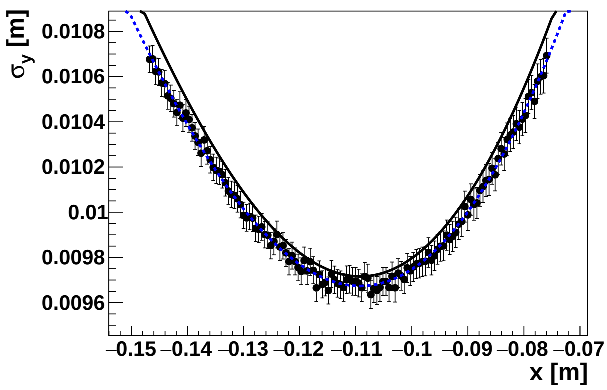

Figure 9: Beam reconstruction for a large beam emittance of 7×10^{-5} m rad *showing the underestimation of the measured vertical beam sizes.*

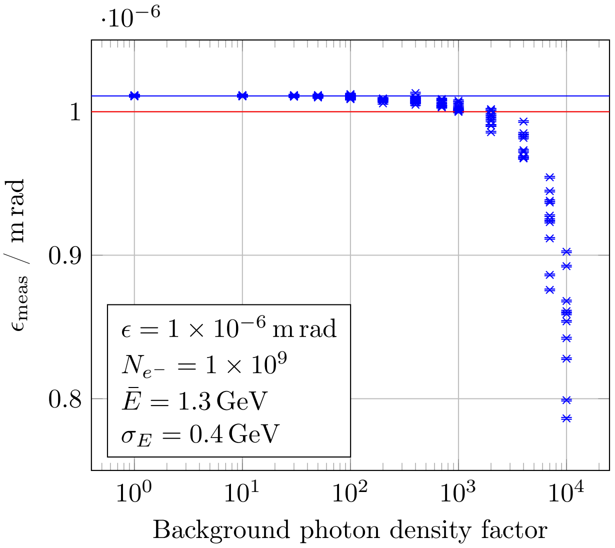

Figure 10: Plot of the measured beam emittance against a factor of the expected background density of 3.415×10^4 photons/m^2

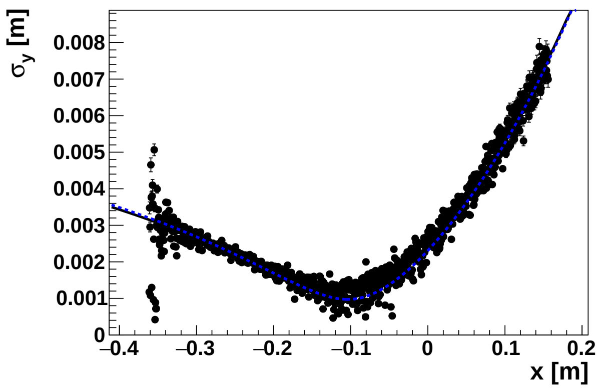

Figure 11: Beam reconstruction for a background 1×10^4 *times the expected background photon density.*

rors are still only a few percent of the measurement. This behaviour reflects how the errors for the background noise were calculated; the error associated with the background photons for each pixel is set to the square root of the number of background photons. This means the fewer the number of incident background photons the screen, the smaller the error. However, the error in the uncertainty of the measurement of the background was not taken into account then scaling the raw signal back into the real shape. This extra error arises from the uncertainty in the measurement of the background photon density when there is no accelerated election beam. To take this into account, this error must be added in quadrature to each pixel.

The upper ranges of this energy spread may also be investigated, however, this is less of a priority. Percentage energy spreads up to 80 % were investigated without signs of alterations to the measured emittance of emittance measurement. It is expected that as the beam energy moves outside the 0.28 GeV to 6 GeV range, emittance measurements will become more erroneous since most of the beam will not hit the screen.

6.3 Input Emittance

Since the emittance is the parameter required to be measured, a reasonably large region around the expected emittance should give precise emittance measurements. The input beam emittance range tested was from 1×10^{-7} m rad to 1×10^{-4} m rad as shown in Figure 8. Emittances below 10^{-5} m rad showed accurate emittance measurements, with the $\sim 10^{-8}$ m rad overestimation of the emittance measuring persisting over this range.

Increasing the emittance of the beam above 10^{-5} m rad results in an underestimation in the measurement of the emittance as well as an increase in the measurement's error. This behaviour is expected. Increasing the emittance of the beam means the spread of the beam on the screen is larger. At emittances above 10^{-5} m rad, a significant proportion of the beam's electrons no longer hit the 6.5 cm tall screen, so particles with the largest transverse momentum no longer contribute to the emittance measurement. Figure 9 displays this effect showing that the shape of the beam on the screen is a lot less focused in the vertical axis and each vertical beam size measurement is underestimated in comparison to the run of expected parameters in Figure 4.

6.4 Background Photons

This background noise is the most likely source of error to change during and between runs, as all other sources of error arise from intrinsic properties of the equipment, or from the setup of the experiment. The background photon noise is expected to be almost insignificant in comparison to the signal of the beam, where the ratio of signal to background photons is expected to be in the order of magnitude 4×10^4. The aim was to find the level of background photon radiation at which the measurement of the emittance would be strongly affected. The expected background density was multiplied by an arbitrary factor until the emitance value deviated from the true value. Figure 10 shows how this factor affects the measurement. Only after the expected background has beed multiplied by a factor of ~ 100 is any effect seen on the measured emittance. Between background factors 10^2 and 10^3 the measured emittance begins to be underestimated and above a background factor of 10^3 the emittance measurement becomes increasingly imprecise with a deviation a few percent at a background factor of 2×10^3, increasing up to 10 % at a background factor of 10^7.

The reasoning for a larger spread in the measured emittance values comes from the background drowning out the signal, that is, the fluctuations of the randomly generated background between the pixels become large enough to distort the shape of the image on the screen. The amount by which the image is distored is not taken into account by the error bars in Figure 10, suggesting that error in the background was not completely accounted for. The absence of this error is propagated to the error of the emittance measurement, as can be seen in Figure 10, as the error significanly underestimates the fluctuations in the measurement. However, these error bars can be inferred from the spread of the measurements since for lower backgrounds all ten runs are closely grouped and for higher backgrounds there is a clear spread of measurement values.

Figure 10, also shows that the emittance measurement is consistently underestimated for large backgrounds. This can be explained by the method of calculating the beam size for a single strip of pixels.

7 Conclusion

The effect of three different experimental parameters were investigated, and the ranges between which the emittance measurements were accurate and reasonably precice were found. Despite the fact that the error measurements were misscalculated, these can be infered from the spread of these measurements. So the behaviour of the emittance measurement with respect to these parameters have been presented.

There still remains many possible combinations of these parameters to be investigated. For example at higher backgrounds, the range of percentage energy spreads where an emittance measurement would be reliable is likely to shift. For this reason, the expected values for all other parameters that were not being investigated were used.

References

[1] I Agapov et al. "BDSIM: A particle tracking code for accelerator beam-line simulations including particle–matter interactions". In: *Nuclear Instruments and Methods in Physics Research Section A: Accelerators, Spectrometers, Detectors and Associated Equipment* 606.3 (2009), pp. 708–712.

[2] Sea Agostinelli et al. "GEANT4 - A simulation toolkit". In: *Nuclear instruments and methods in physics research section A: Accelerators, Spectrometers, Detectors and Associated Equipment* 506.3 (2003), pp. 250–303.

[3] R. Barate et al. "Search for the standard model Higgs boson at LEP". In: *Phys. Lett.* B565 (2003), pp. 61–75. DOI: 10.1016/S0370-2693(03)00614-2. arXiv: hep-ex/0306033 [hep-ex].

[4] Ties Behnke et al. "The International Linear Collider Technical Design Report - Volume 1: Executive Summary". In: (2013). arXiv: 1306.6327 [physics.acc-ph].

[5] R. Brun and F. Rademakers. "ROOT: An object oriented data analysis framework". In: *Nucl. Instrum. Meth.* A389 (1997), pp. 81–86. DOI: 10.1016/S0168-9002(97)00048-X.

[6] Jean Buon. "Beam phase space and emittance". In: *CERN European Organization for Nuclear Research-Reports-CERN* (1994), pp. 89–89.

[7] Allen Caldwell et al. "Proton Driven Plasma Wakefield Acceleration". In: *Nature Phys.* 5 (2009), pp. 363–367. DOI: 10.1038/NPHYS1248, 10.1038/nphys1248. arXiv: 0807.4599 [physics.acc-ph].

[8] CMS Collaboration. "First measurement of the differential cross section for ttbar production in the dilepton final state at sqrts = 13 TeV". In: (2015).

[9] *Hardware Guide for the iStar Intensified sCMOS camera*. Version 1 rev 19. ANDOR an Oxford Instruments company. Andor Technology Ltd., 7 Millennium Way, Springvale Business Park, Belfast, BT12 7AL, Northern Ireland, Sept. 2016.

[10] Naveen Kumar, Alexander Pukhov, and Konstantin Lotov. "Self-modulation instability of a long proton bunch in plasmas". In: *Physical review letters* 104.25 (2010), p. 255003.

[11] Wim P. Leemans et al. "GeV electron beams from a cm-scale accelerator". In: *Nature Phys.* 2 (2006), pp. 696–699. DOI: 10.1038/nphys418.

[12] Lucie Linssen et al. "Physics and Detectors at CLIC: CLIC Conceptual Design Report". In: (2012). DOI: 10.5170/CERN-2012-003. arXiv: 1202.5940 [physics.ins-det].

[13] KV Lotov et al. "Natural noise and external wakefield seeding in a proton-driven plasma accelerator". In: *Physical Review Special Topics-Accelerators and Beams* 16.4 (2013), p. 041301.

[14] W. Lu et al. "Generating multi-GeV electron bunches using single stage laser wakefield acceleration in a 3D nonlinear regime". In: *Phys. Rev. ST Accel. Beams* 10 (2007), p. 061301. DOI: 10.1103/PhysRevSTAB.10.061301. arXiv: physics/0612227 [physics].

[15] E. Öz, F. Batsch, and P. Muggli. "An accurate Rb density measurement method for a plasma wakefield accelerator experiment using a novel Rb reservoir". In: *Nucl. Instrum. Meth.* A829 (2016), pp. 321–325. DOI: 10.1016/j.nima.2016.02.005. arXiv: 1511.08763 [physics.ins-det].

[16] Erdem Öz, Fabian Batsch, and Patric Muggli. "A Novel Laser Ionized Rb Plasma Source for Plasma Wakefield Accelerators". In: *Proceedings, 5th International Particle Accelerator Conference (IPAC 2014): Dresden, Germany, June 15-20, 2014*. 2014, TUPME073. URL: http://jacow.org/IPAC2014/papers/tupme073.pdf.

[17] Carl Siemon et al. "Laser-seeded modulation instability in a proton driver plasma wakefield accelerator". In: *Physics of Plasmas (1994-present)* 20.10 (2013), p. 103111.

[18] A. A. Sokolov and I. M. Ternov. "Synchrotron radiation". In: *Akademia Nauk SSSR, Moskovskoie Obshchestvo Ispytatelei prirody. Sektsia Fiziki. Sinkhrotron Radiation, Nauka Eds., Moscow, 1966 (Russian title: Sinkhrotronnoie izluchenie), 228 pp.* (1966).

[19] T. Tajima and J. M. Dawson. "Laser electron accelerator". In: *Phys. Rev. Lett.* 43 (1979), pp. 267–270. DOI: 10.1103/PhysRevLett.43.267.

[20] J. Vieira et al. "Ion motion in the wake driven by long particle bunches in plasmas". In: *Phys. Plasmas* 21 (2014), p. 056705. DOI:

10.1063/1.4876620. arXiv: 1409.4328 [physics.plasm-ph].

[21] J. Vieira et al. “The ion motion in self-modulated plasma wakefield accelerators”. In: *Phys. Rev. Lett.* 109 (2012), p. 145005. DOI: 10.1103/PhysRevLett.109.145005. arXiv: 1208.3242 [physics.plasm-ph].

[22] Helmut Wiedemann. *Particle accelerator physics I*. Berlin, Germany: Springer, 1999. ISBN: 9783540490432, 9783662038277. DOI: 10.1007/978-3-662-03827-7. URL: http://www.springer.com/us/book/9783662038277.